



HAL
open science

Composite Mn-Co electrode materials for supercapacitors: Why the precursor's morphology matters!

Ronan Invernizzi, Alexia Lemoine, Lénaïc Madec, François Weill, Marie-Anne Dourges, Céline Tang, Domitille Giaume, Isabelle Baraille, P.-L. Taberna, Delphine Flahaut, et al.

► **To cite this version:**

Ronan Invernizzi, Alexia Lemoine, Lénaïc Madec, François Weill, Marie-Anne Dourges, et al.. Composite Mn-Co electrode materials for supercapacitors: Why the precursor's morphology matters!. *Nanoscale Advances*, 2022, 4 (23), pp.5089-5101. 10.1039/d2na00616b . hal-03824766

HAL Id: hal-03824766

<https://hal.science/hal-03824766>

Submitted on 21 Oct 2022

HAL is a multi-disciplinary open access archive for the deposit and dissemination of scientific research documents, whether they are published or not. The documents may come from teaching and research institutions in France or abroad, or from public or private research centers.

L'archive ouverte pluridisciplinaire **HAL**, est destinée au dépôt et à la diffusion de documents scientifiques de niveau recherche, publiés ou non, émanant des établissements d'enseignement et de recherche français ou étrangers, des laboratoires publics ou privés.

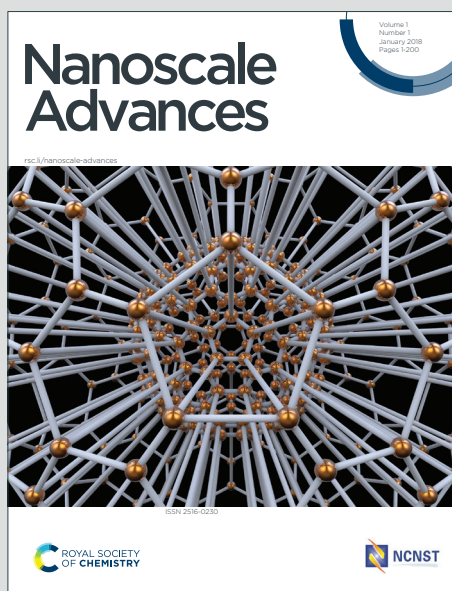


Distributed under a Creative Commons Attribution - NonCommercial - NoDerivatives 4.0 International License

Nanoscale Advances

Accepted Manuscript

This article can be cited before page numbers have been issued, to do this please use: R. Invernizzi, A. Lemoine, L. Madec, F. Weill, M. Dourges, C. Tang, D. Giaume, I. Baraille, P. Taberna, D. Flahaut, J. Olchowka and L. Guerlou-Demourgues, *Nanoscale Adv.*, 2022, DOI: 10.1039/D2NA00616B.



This is an Accepted Manuscript, which has been through the Royal Society of Chemistry peer review process and has been accepted for publication.

Accepted Manuscripts are published online shortly after acceptance, before technical editing, formatting and proof reading. Using this free service, authors can make their results available to the community, in citable form, before we publish the edited article. We will replace this Accepted Manuscript with the edited and formatted Advance Article as soon as it is available.

You can find more information about Accepted Manuscripts in the [Information for Authors](#).

Please note that technical editing may introduce minor changes to the text and/or graphics, which may alter content. The journal's standard [Terms & Conditions](#) and the [Ethical guidelines](#) still apply. In no event shall the Royal Society of Chemistry be held responsible for any errors or omissions in this Accepted Manuscript or any consequences arising from the use of any information it contains.

Composite Mn-Co electrode materials for supercapacitors: Why the precursor's morphology matters!

View Article Online
DOI: 10.1039/C2NA00616B

Ronan Invernizzi,^{a,b} Alexia Lemoine,^c Lénaïc Madec,^{b,c} François Weill,^{a,b} Marie-Anne Dourges,^d Céline Tang,^{a,b,e} Domitille Giaume,^{b,e} Isabelle Baraille,^{b,c} Pierre Louis Taberna,^{b,f,g} Delphine Flahaut,^{b,c} Jacob Olchowka,^{*a,b,f} Liliane Guerlou-Demourgues^{*a,b,f}

^a Université Bordeaux, CNRS, Bordeaux INP, ICMCB UMR 5026, F-33600 Pessac, France.

^b RS2E, Réseau Français sur le Stockage Electrochimique de l'Energie, FR CNRS #3459, F-80039 Amiens Cedex 1, France.

^c CNRS/Univ. Pau & Pays Adour / E2S UPPA, Institut des Sciences Analytiques et de Physicochimie pour l'Environnement et les Matériaux – UMR 5254, 64000 Pau, France.

^d Institut des Sciences Molaires, Univ. Bordeaux, UMR 5255, F-33405 Talence, France

^e Chimie-ParisTech, PSL Research University, CNRS Institut de Recherche de Chimie-Paris (IRCP), 75005 Paris, France

^f ALISTORE-ERI European Research Institute, FR CNRS #3104, Amiens, F-80039 Cedex 1, France.

^g CIRIMAT, Université de Toulouse, CNRS, Université Toulouse 3 – Paul Sabatier, 118 Route de Narbonne, 31062 Toulouse Cedex 9, France

Abstract :

In the energy storage field, an electrode material must possess both good ionic and electronic conductivities to perform well, especially when high power is needed. In this context, the development of composite electrode materials combining an electrochemically active and good ionic conductor phase with an electronic conductor appears as a perfectly adapted approach to generate a synergetic effect and optimize the energy storage performance. In this work, three layered MnO₂ phases with various morphologies (veals, nanoplatelets and microplatelets) were associated with electronic conductor cobalt oxyhydroxides with different platelet sizes (~20 nm vs 70 nm wide), to synthesize 6 different composites by exfoliation and restacking process. The influence of precursors' morphology on the distribution between the Mn and Co objects within the composites was carefully investigated and correlated to the electrochemical performance of the final restacked material. Overall, the best performing restacked composite was obtained by combining MnO₂ possessing a veal morphology with the



smallest cobalt oxyhydroxide nanoplatelets, leading to the most homogeneous distribution of the Mn and Co objects at the nanoscale. More generally, the aim of this work is to understand how the size and morphology of the precursors building blocks influence their distribution homogeneity within the final composite and to find the most compatible building blocks to reach a homogenous distribution at nanoscale.

Keywords: composite; distribution homogeneity; exfoliation and restacking; morphology design; supercapacitors.

Introduction

Driven by the transition towards sustainable but intermittent energy production along with the emergence of electric vehicles, the development of safe, reliable and high-performance energy storage systems turns into one of the most important challenge facing the scientific community.^{1,2} For instance, many efforts are currently done to increase the energy density of batteries with the perspective of boosting the driving range of electric vehicles.³ Nevertheless, these high energy density batteries are not well-adapted to high power applications such as for energy recovery during braking or grid power buffering, due to the diffusion limited processes characteristic of these systems. Electrochemical double-layer capacitors (EDLC), thanks to their capacitive storage, are able to meet the needs in term of time response for these power applications. However their capacity is too low for many practical purposes.^{4,5}

Thus, the pseudocapacitive systems appear as the ideal alternative to meet at the same time high power and suitable energy density.⁶ Their fast and reversible near-surface Faradaic reactions to store charges allow surpassing the capacity limitation of EDLC while keeping fast time responses.^{7,8} Among the various pseudocapacitive electrode materials, MnO₂ is one of the most studied thanks to its abundance, high theoretical capacity, stability in aqueous electrolyte and low price.^{9–12} Nonetheless, the manganese oxide phases possess a poor electronic conductivity that, in practice, strongly limits their rate capability.^{13,14}

To counterbalance this limiting aspect, two ways are mainly investigated in the literature. The first one targets the nanostructuring of MnO₂ to both increase the specific surface area and thus, the number of surface redox active sites and to shorten the electron pathways to improve the kinetics.¹⁵ To do so, plenty of different synthesis approaches have been reported these last years such as coprecipitation, template assisted synthesis, hydro/solvothermal synthesis and chemical vapor deposition leading to original morphologies and often enhanced performance.^{16–21} The second approach widely studied consists in combining MnO₂ with an



electronic conductive material leading to hybrid or composite electrode materials.^{22,23} The development of hybrid compounds made of MnO₂ with an electronic conductive carbon material such as graphene, carbon nanotubes or nanofibers or with a conductive polymer such as PEDOT or PPy appears as a well-adapted method as they are easy to synthesize, exhibits excellent chemical and electrochemical stability, and offers the possibility to obtain self-supported electrodes.^{21,24} Another efficient approach to boost the power ability is to synthesize MnO₂ – conductive metal composites such as composites with transition metal oxides/carbides or with metallic nanoparticles.^{25–27} Following this idea, Tang et al. recently developed an original approach to combine lamellar manganese oxides (birnessite δ-MnO₂) with layered non-stoichiometric cobalt oxyhydroxides (β3-CoOOH) by exfoliation/restacking processes.²⁸ This cobalt phase displays indeed a very high electronic conductivity (~ 1 S/cm at room temperature) due to the presence of Co⁴⁺ in the CoO₂ slabs.^{29,30} The authors investigated the optimal molar ratio between the pseudocapacitive birnessite MnO₂ and the electronic conductive β3-CoOOH phase to reach the best capacity retention at high rates. It was found that a ratio Mn:Co of 3:1 exhibits the greatest synergetic effect between both phases leading to a composite with better rate performance than simple manganese oxide or than MnO₂ mixed with carbon black.³¹ Based on these very promising results, we decided to study in more details the distribution scale of MnO₂ and β3-CoOOH within the composite as well as the influence of precursors' morphology on the homogeneity and electrochemical performance of the final restacked materials. More generally, the aim of this work is to understand how the size and morphology of the precursor building blocks influence their distribution homogeneity within the final composite and to find the most compatible building blocks to reach a homogenous distribution at nanoscale.

To do so, we synthesize birnessite precursors with three different morphologies (veils, big platelets and small platelets) and two cobalt oxyhydroxide precursors with platelets of different sizes (around 70 nm wide and 20 nm wide) to finally obtain 6 different composites with the same optimal Mn:Co ratio of 3:1. The distribution between the Mn and Co objects within the composites was thoroughly investigated by nitrogen adsorption, nano-Augur spectroscopy, transmission electronic microscopy and correlated to the specific surface area of the composites as well as their energy storage performance at high rates.



EXPERIMENTAL

View Article Online
DOI: 10.1039/D2NA00616B

Preparation of cobalt oxyhydroxide precursors

Method 1: the β (III) cobalt oxyhydroxide phase is prepared by precipitation at constant pH 14 (reverse precipitation). First, 3.18 g of $\text{Co}(\text{NO}_3)_2 \cdot 6\text{H}_2\text{O}$ (Sigma Aldrich) are dissolved in 300 mL of distilled water. Then, the nitrate solution is slowly added into 11 mL of 2M NaOH under stirring. Immediately after the addition of the nitrate solution, a blue (α - $\text{Co}(\text{OH})_2$) precipitate appears, it quickly turns pink (β (II)- $\text{Co}(\text{OH})_2$) and finally turns to brown (partially oxidized cobalt hydroxide). To speed up the oxidation process of the freshly made cobalt hydroxide, 7.5 mL (3 times the required volume) of NaClO (48 °Cl) are added dropwise to the solution that becomes black. The final solution is stirred during 36 hours at room temperature, centrifuged several times at 4000 rpm until neutral pH, and dried at 45 °C for one day.

Method 2: the β (III) cobalt oxyhydroxide phase is synthesized by forward precipitation at increasing pH (the pH value increases from 6 to 10 during the precipitation) : 11 mL of 2M NaOH solution is slowly added into the nitrate solution (3.18 g in 300 mL of distilled water) before the same oxidation, centrifugation and drying steps as seen for method 1.²⁹

The pure β (III) cobalt oxyhydroxides prepared by method 1 and by method 2 are designated by β 3-pH₁₄ and β 3-pH₇ respectively.

Preparation of manganese precursors

Platelets and veals manganese oxides

First, 1.69 g of $\text{MnSO}_4 \cdot \text{H}_2\text{O}$ (Sigma Aldrich) is dissolved into 30 mL of distilled water under stirring. 30 mL of 6M NaOH/KOH (Sigma Aldrich) are then added into the previous solution; the solution turns immediately to orange/light brown, which corresponds to the formation of $\text{Mn}(\text{OH})_2$. To oxidize the Mn ions to an approximate oxidation degree of 3.7, 1.89 g of $\text{K}_2\text{S}_2\text{O}_8$ (Sigma Aldrich) is added over a period of 50 minutes. The precipitate slowly turns to dark brown. The suspension is then aged under stirring for 30 minutes and washed/centrifuged few times until neutral pH. The recovered powder is dried at 50°C for two days. The syntheses leads to P- MnO_2 (platelets) when NaOH was used as precipitating agent and V- MnO_2 (veals) when using KOH.



High temperature manganese oxide

1 g of KMnO_4 (Sigma Aldrich) is placed into an alumina boat and heated in an oven for 5 hours at 800°C with heating and cooling ramp rates of $5^\circ\text{C}/\text{min}$. After thermal decomposition, the powder is washed with deionized water to remove the two impurity phases K_2MnO_4 and K_3MnO_4 that pass into solution (blue/green solution).³² The resulting sample is dried two days at 50°C . It is designated as HT-MnO_2 (High Temperature).

Protonation of manganese oxides

In order to be easily exfoliated, the manganese oxides need to be protonated, which is performed through an exchange of initial sodium/potassium ions by protons.³³ For that purpose, 0.5 g of the powder is suspended into a solution of 0.1 M HCl during 3 days under stirring, to replace the majority of the alkaline ions by protons. The powders are recovered by centrifugation and washed few times until neutral pH of the supernatant. The protonation of $V\text{-MnO}_2$, $P\text{-MnO}_2$ and HT-MnO_2 leads to $V_H\text{-MnO}_2$, $P_H\text{-MnO}_2$ and $\text{HT}_H\text{-MnO}_2$ respectively.

Exfoliation

The protonated Mn and Co oxides are separately suspended into a solution of water and tetrabutylammonium hydroxide (TBAOH). The TBAOH solution is added to respect a $\text{H}^+:\text{TBA}^+$ molar ratio of 1:10 for manganese phases and 1:2 for cobalt ones. The suspensions are sonicated 3 times during 1 hour (with 0.5 s /0.5 s (pulse in/off)) and aged under stirring 20-30 days. They are finally centrifuged at 4000 rpm during 5 minutes. As the outcome of the treatment, part of the material flocculates at the bottom of the recipient whereas the other part remains suspended in the supernatant part. The latter is recovered and the resulting colloidal suspension will be further used for the restacking step.

Synthesis of restacked materials

The molar ratio between the manganese and cobalt suspensions is set to 3, which according to the previous work of Tang et al., should be the optimal ratio for high rate performance.²⁸ Each colloidal suspension of manganese and cobalt is adjusted at $\text{pH} = 4.5$ by gradual addition of nitric acid. The volume of the two suspensions is adjusted to 200 mL before these latter are slowly transferred with a peristaltic pump into a solution of 20 mL of nitric acid at $\text{pH} = 4.5$. When they come into contact, the different nano-objects should flocculate on top of each other considering that at $\text{pH} = 4.5$, the surface of Mn objects is negatively charged whereas that of Co particles is positively charged. The optimal pH conditions for the restacking step were



determined by zeta potential measurements, as detailed in the Supporting Information Figure S1. Finally, the restacked materials are recovered by centrifugation after being washed several times until neutral pH.

X-ray diffraction

The X-ray diagrams for all samples were recorded on a Philips PANalytical X'Pert Pro equipped with a copper source ($\lambda_{K\alpha 1} = 0.1540$ nm et $\lambda_{K\alpha 2} = 0.1544$ nm). The powder diffraction patterns were recorded for about 2 h in the 10–80° (2 θ) angular range, with a 0.02° (2 θ) step size and a 2.022° (2 θ) active width in the detector. The size of the coherent domains of the different phases was calculated using the Scherrer equation from (00*l*) reflections. The attribution and the purity of the phases were confirmed by comparison with reference peaks from PDF 00-042-1317 (MnO₂ birnessite) and 07-0169 (H_xCoO₂)

Specific Surface Area and Porosity

Surface area and pore structure were explored by recording nitrogen adsorption isotherms at 77 K with Micromeritics 3Flex equipment. Before analysis, the samples were degassed at 60 °C under vacuum for 15 h to reach a pressure less than 10 μ m Hg.

The specific surface area was obtained using the BET equation applied between 0.01 and 0.25 relative pressure (p/p_0).³⁴

Restacked materials cross-section preparation, scanning electron microscopy (SEM), Auger Electron Spectroscopy (AES) and Scanning Auger Microscopy (SAM)

To analyze both the surface and the bulk of the restacked materials, samples were cross-sectioned. For this, the sample powders were mixed with a silver conducting epoxy resin (to ensure a low charge effect during acquisition) and then deposited on a silicon wafer. The wafer and the powder-epoxy mixture were cut with an Ar⁺ ion beam of 6 keV and about 150 μ A at 1.10⁻⁴ Pa during 5 hours with a JEOL IB-09010CP cross polisher located in a glove box under an N₂ controlled atmosphere. The cutting depth of the samples is 150 μ m. The cross-sectioned samples were then transferred from the glove box to the Auger spectrometer for analysis using a transfer vessel to avoid any contact with air.

An Auger JEOL JAMP 9500F spectrometer was used for Scanning Electron Microscopy (SEM), Auger Electron Spectroscopy (AES) and Scanning Auger Microscopy (SAM). The SEM images of restacked materials were carried out under Ultra High Vacuum conditions (< 2x10⁻⁷Pa). An acceleration voltage of 20 kV and a current beam of 3 or 4 nA was used for both SEM and AES/SAM. Accordingly, the probe size is about 20 nm (which corresponds to a



spatial resolution for SAM of about 30 nm) and the probing depth is about 3 nm. The analysis was performed at 30° tilt to prevent charging effect.

The AES survey spectra were recorded between 25 and 1000 eV with a step of 1 eV. SAM images (elemental 2D distribution) have been represented using “peak minus background” (P-B) of the Auger intensity for a transition ($dE/E = 0.5\%$).

For AES survey spectra and SAM images, an “auto probe tracking” was used to control any potential drift during analyzes.

Transmission Electron Microscopy (TEM)

The samples were placed on a formavar/carbon supported film on a copper grid. Images of each sample were obtained with a JEOL 2100 transmission electron microscope (JEOL, Tokyo, Japan).

Electrochemistry

The active material was mixed with carbon black and polytetrafluoroethylene in a weight ratio of 80/15/5 to prepare the working electrodes. The electrode was then pressed at 5 bars on stainless steel grid for one minute. The mass loading of the electrodes is ~ 10 mg/cm². Electrochemical measurements were carried out in a solution of 0.5 M K₂SO₄ in a 3-electrodes configuration at 25°C. The reference electrode was an Ag/AgCl electrode and as the counter electrode, a platinum wire was used.

EIS measurements

For EIS measurements, the electrodes were pressed on stainless steel current collector which was gold coated-sputtering in order to suppress/minimize the contact impedance between the current collector and the active material. The EIS measurements of the composites were performed at potentials of 0.2, 0.3, 0.4, 0.5 and 0.6 V vs Ag/AgCl, in 0.5 M K₂SO₄. For the measurements, a perturbation of 5 mV was used in a frequency range from 10 kHz down to 10 mHz was set.



RESULTS AND DISCUSSION

View Article Online
DOI: 10.1039/D2NA00616B

1) Structural characterization of the restacked composites compared to the cobalt and manganese precursors

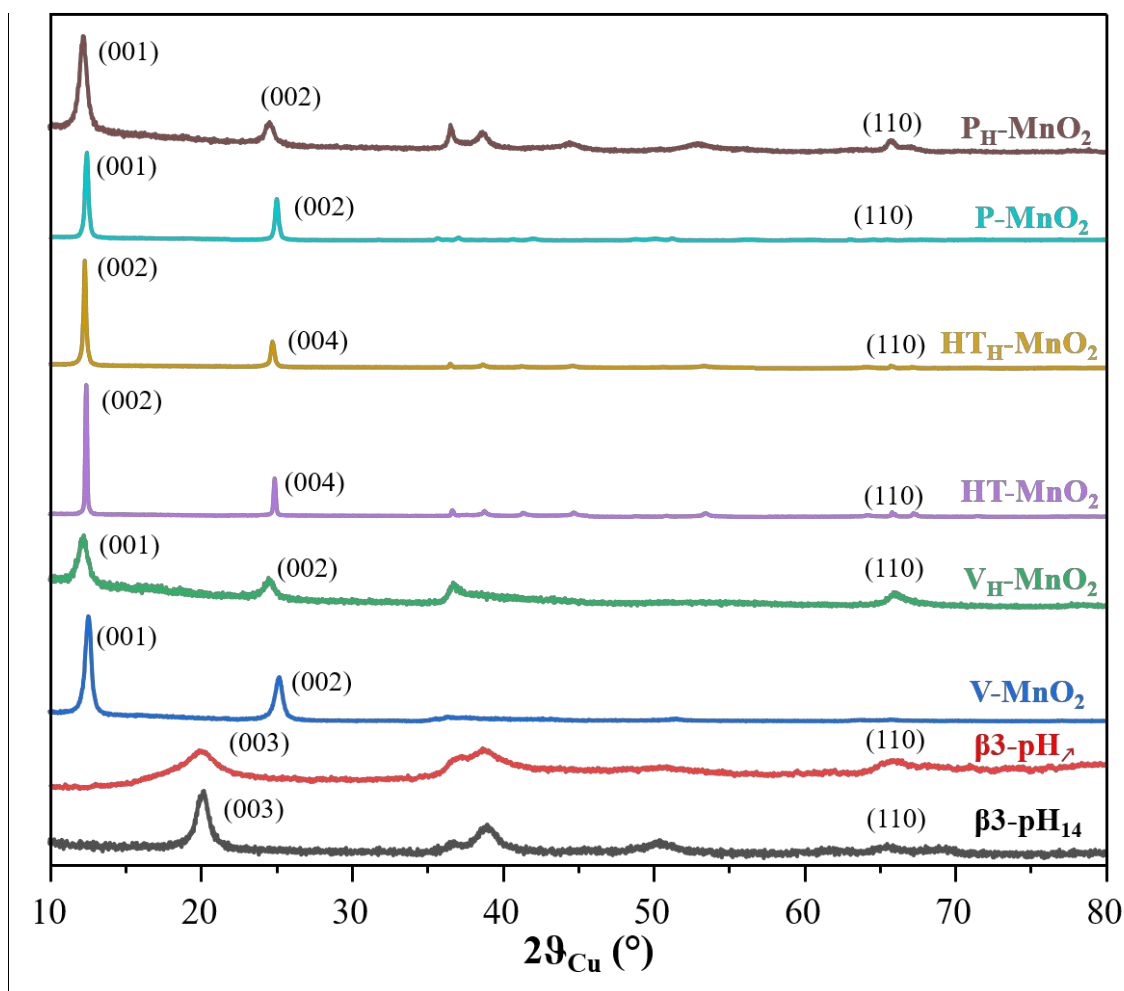
Structural characterization of the precursors

Figure 1. X-ray diffraction patterns of the cobalt and manganese precursors: $\beta 3\text{-pH}_{14}$ (black), $\beta 3\text{-pH}_7$ (red), $V\text{-MnO}_2$ (blue), $V_H\text{-MnO}_2$ (green), $HT\text{-MnO}_2$ (purple), $HT_H\text{-MnO}_2$ (yellow), $P\text{-MnO}_2$ (cyan) and $P_H\text{-MnO}_2$ (brown).

The X-ray diffraction patterns of the initial precursors and the corresponding protonated phases are shown in Figure 1 whereas their accurate chemical compositions are listed in Table S1. The diffractograms of all samples can be indexed with a hexagonal cell (except for $V\text{-MnO}_2$ and $P\text{-MnO}_2$ which display a monoclinic distortion) and are typical of lamellar materials; the inter-reticular distance corresponding to the diffraction peak at the lowest angle gives the interslab distance (between two $(\text{Mn/Co})\text{O}_2$ slabs) while the distance of the (110) reflection is equal to half the Metal-Metal distance (cell-parameter “ a_{hex} ”) in the hexagonal slab.



The diagrams of the two cobalt oxyhydroxides $\beta 3\text{-pH}_{14}$ and $\beta 3\text{-pH}_7$ show the signature of pure $\beta 3\text{-CoOOH}$ phases.³⁵ However, the XRD pattern of $\beta 3\text{-pH}_7$ reveals smaller coherent domains as compared with $\beta 3\text{-pH}_{14}$ due to broader and less defined diffraction peaks. The size of the coherent domains is estimated along the [001] direction as around 10 nm for $\beta 3\text{-pH}_{14}$ against 3 nm for $\beta 3\text{-pH}_7$.

V-MnO₂, P-MnO₂ and HT-MnO₂ exhibit similar X-ray diffraction patterns that correspond to birnessite phase $\delta\text{-MnO}_2$. However, V-MnO₂ shows less defined and larger diffraction peaks than the two other birnessite phases, suggesting a crystallinity loss. Indeed, V-MnO₂ displays coherent domains of 12 nm, whereas those of P-MnO₂ and HT-MnO₂ are estimated with the (001) reflection at around 58 nm and 119 nm respectively. The asymmetric profile of (10 l) and (11 l) diffraction peaks for V-MnO₂ is characteristic of a turbostratic stacking or the presence of several stacking polytypes as it is commonly observed in birnessite materials.³⁶ The sodium birnessite P-MnO₂ exhibits a larger interlayer distance than for the two potassium birnessites (7.13 Å vs. 7.08 Å for HT-MnO₂ and V-MnO₂).^{32,37} Considering the ionic radius of sodium and potassium ions (0.99 Å and 1.51 Å respectively), this could first appear as counter intuitive.³⁸ However, the higher polarizing effect of Na⁺ versus K⁺ leads to a larger hydration shell for Na⁺, even for alkaline ions in the confined interlayer of birnessite, which thus, induces a higher interlayer space for P-MnO₂.^{39,40} This is supported by the larger quantity of intercalated water molecules for P-MnO₂ compared to the other two manganese oxides (Table S1).

A comparison of the birnessite phases before and after protonation shows that the protonation step induces i) a shift of the (00 l) reflections towards lower angles, revealing an increase of the interlayer spacing (Figure 1) and ii) a drastic drop of alkaline concentration in parallel to an increase of protons content (Table S1). These evolutions confirm the successful exchange of alkaline for proton. The protonation step does not influence the coherent domains of HT-MnO₂ and V-MnO₂, which remain around 119 nm and 12 nm respectively. On the other hand, the size of the coherent domains decreases by more than a factor 2 after protonation for P-MnO₂ (from 58 nm to 25 nm), which suggests that the crystallites of P-MnO₂ are already exfoliated during the protonation step, since the coherent domain calculated along the [001] direction is directly related to the number of stacked metal oxide slabs in a crystallite.

Structural characterization of the restacked composites

By combining three different protonated birnessites (V_H-MnO₂, P_H-MnO₂ and HT_H-MnO₂) and the two cobalt oxyhydroxides ($\beta 3\text{-pH}_{14}$ and $\beta 3\text{-pH}_7$), six restacked materials were obtained. It



should be noticed that all of them exhibit the targeted molar ratio Mn:Co of 3:1, as confirmed by ICP-OES measurements (Table S2). The XRD patterns of the final restacked materials (purple, yellow and cyan curves) are shown in Figure 2 along with the corresponding cobalt (black curve) and protonated manganese precursors (red, green and blue curves). Figure 2a) and 2b) show restacked materials obtained with $\beta 3\text{-pH}_{14}$ and $\beta 3\text{-pH}_7$ respectively.

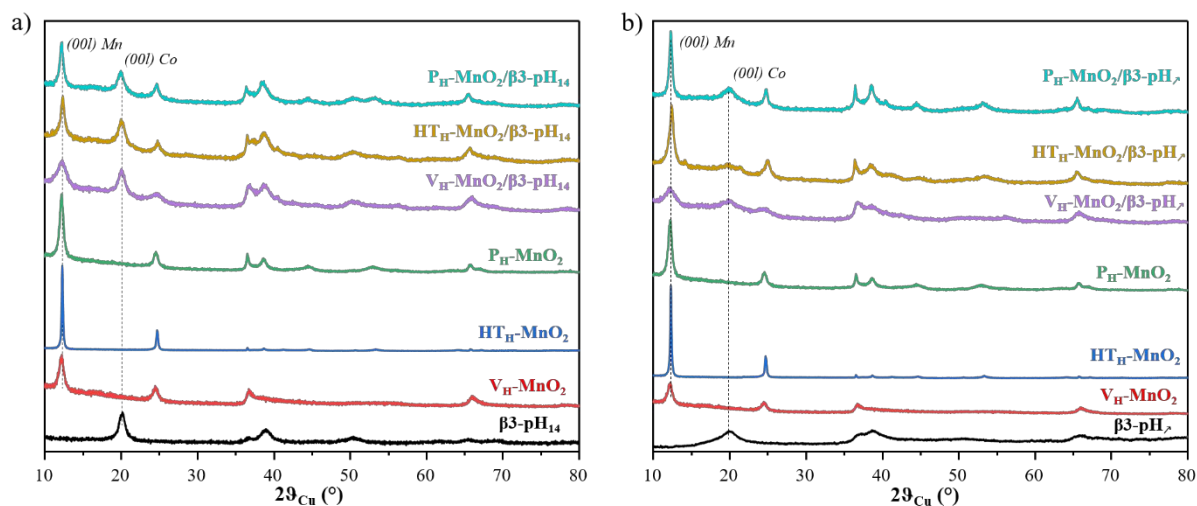


Figure 2 : X-ray diffraction patterns of a) $\beta 3\text{-pH}_{14}$ (black), $V_H\text{-MnO}_2$ (red), $HT_H\text{-MnO}_2$ (blue), $P_H\text{-MnO}_2$ (green), $V_H\text{-MnO}_2/\beta 3\text{-pH}_{14}$ (purple), $HT_H\text{-MnO}_2/\beta 3\text{-pH}_{14}$ (yellow), $P_H\text{-MnO}_2/\beta 3\text{-pH}_{14}$ (cyan) and b) $\beta 3\text{-pH}_7$ (black), $V_H\text{-MnO}_2$ (red), $HT_H\text{-MnO}_2$ (blue), $P_H\text{-MnO}_2$ (green), $V_H\text{-MnO}_2/\beta 3\text{-pH}_7$ (purple), $HT_H\text{-MnO}_2/\beta 3\text{-pH}_7$ (yellow), $P_H\text{-MnO}_2/\beta 3\text{-pH}_7$ (cyan).

The XRD patterns show that every restacked material is composed of two phases: a cobalt oxyhydroxide and a protonated manganese oxide. In order to better understand the phenomena that happened during the experimental procedure, the coherent domain sizes of cobalt and manganese phases were compared before and after the exfoliation/restacking step. Generally speaking, a decrease of coherent domain of a phase along the [001] direction in the final material means that the number of stacked layers within a crystallite is reduced, which suggests that an exfoliation has occurred. If, by contrast, the sizes of coherent domains remain unchanged between the precursors and the restacked materials, it is highly likely that no exfoliation happened and that the crystallites and/or the primary particles might be just separated or dis-agglomerated.

According to the coherent domain values given in Table 1, whatever the restacked material, there is no significant change in the size of crystallites along the [001] direction for the cobalt phases, meaning that the cobalt phases are probably not exfoliated. For manganese objects there are two types of behavior. The long-term stirring of $P_H\text{-MnO}_2$ in the TBAOH solution followed



by a restacking step do not induce further exfoliation, the coherent domains remain unchanged around 25 nm (Table 1). On the other hand, $V_{\text{H}}\text{-MnO}_2$ and $\text{HT}_{\text{H}}\text{-MnO}_2$ exhibit smaller coherent domains in the final restacked materials (12 nm and 119 nm for the precursors versus 8 nm and 28 or 37 nm after the restacking, respectively), meaning that in this case there is a real exfoliation of MnO_2 crystallites.

Table 1: Size of the coherent domains calculated with Scherrer equation on the (001) reflection peaks for Mn oxide and Co oxyhydroxide inside the restacked materials and in brackets for the precursors.

Sample	Size of the coherent domains of Mn oxide calculated from (001) reflection peak (nm)	Size of the coherent domains of Co oxyhydroxide calculated from (001) reflection peak (nm)
$V_{\text{H}}\text{-MnO}_2/\beta\text{3-pH}_{14}$	8 - (12)	9 - (10)
$P_{\text{H}}\text{-MnO}_2/\beta\text{3-pH}_{14}$	25 - (25)	10 - (10)
$\text{HT}_{\text{H}}\text{-MnO}_2/\beta\text{3-pH}_{14}$	28 - (119)	9 - (10)
$V_{\text{H}}\text{-MnO}_2/\beta\text{3-pH}_{\gamma}$	8 - (12)	3 - (3)
$P_{\text{H}}\text{-MnO}_2/\beta\text{3-pH}_{\gamma}$	25 - (25)	3 - (3)
$\text{HT}_{\text{H}}\text{-MnO}_2/\beta\text{3-pH}_{\gamma}$	37 - (119)	3 - (3)

Specific surface area of the precursors and the restacked composites

These conclusions are supported by the evolution of materials specific surface area (SSA) obtained from BET measurements (Figure 3 and S2). The increase of the SSA of restacked materials containing $V_{\text{H}}\text{-MnO}_2$ and $\text{HT}_{\text{H}}\text{-MnO}_2$ ($V_{\text{H}}\text{-MnO}_2/\beta\text{3-pH}_{14}$, $V_{\text{H}}\text{-MnO}_2/\beta\text{3-pH}_{\gamma}$, $\text{HT}_{\text{H}}\text{-MnO}_2/\beta\text{3-pH}_{14}$ and $\text{HT}_{\text{H}}\text{-MnO}_2/\beta\text{3-pH}_{\gamma}$) as compared to the SSA of initial precursors confirms the exfoliation of these two manganese precursors during the synthesis (Figure 3). For instance, the SSA of $V_{\text{H}}\text{-MnO}_2/\beta\text{3-pH}_{14}$ reaches $121 \text{ m}^2/\text{g}$ whereas those of $V_{\text{H}}\text{-MnO}_2$ and $\beta\text{3-pH}_{14}$ are only of $85 \text{ m}^2/\text{g}$ and $77 \text{ m}^2/\text{g}$ respectively. Similarly, the restacked $\text{HT}_{\text{H}}\text{-MnO}_2/\beta\text{3-pH}_{\gamma}$ composite displays a SSA of $106 \text{ m}^2/\text{g}$ whereas a simple mixing of both precursors with a ratio $\text{HT}_{\text{H}}\text{-MnO}_2:\beta\text{3-pH}_{\gamma}$ of 3:1 would theoretically give a composite with SSA of only $53.5 \text{ m}^2/\text{g}$ ($\frac{3}{4} \cdot 18 + \frac{1}{4} \cdot 160 = 53.5 \text{ m}^2 \cdot \text{g}^{-1}$). On the other hand, there is no significant and unexpected change in the specific surface area between $P_{\text{H}}\text{-MnO}_2$ and the restacked $P_{\text{H}}\text{-MnO}_2/\beta\text{3-pH}_{14}$ and $P_{\text{H}}\text{-MnO}_2/\beta\text{3-pH}_{\gamma}$ (Figure 3) which supports that $P_{\text{H}}\text{-MnO}_2$ is not exfoliated. The larger SSA for $P_{\text{H}}\text{-MnO}_2/\beta\text{3-pH}_{\gamma}$ compared to $P_{\text{H}}\text{-MnO}_2$ ($82 \text{ m}^2/\text{g}$ vs $60 \text{ m}^2/\text{g}$) is due to the high specific surface



area of the $\beta 3\text{-pH}_7$ cobalt oxyhydroxide, present with a molar ratio of 25% in the composite material. Finally, by comparing the SSA of the different composites, it clearly appears that those built with manganese oxides possessing a veil morphology, $V_{\text{H}}\text{-MnO}_2$, exhibit the largest specific surfaces within the series and present the higher mesoporosity (Figure S3).

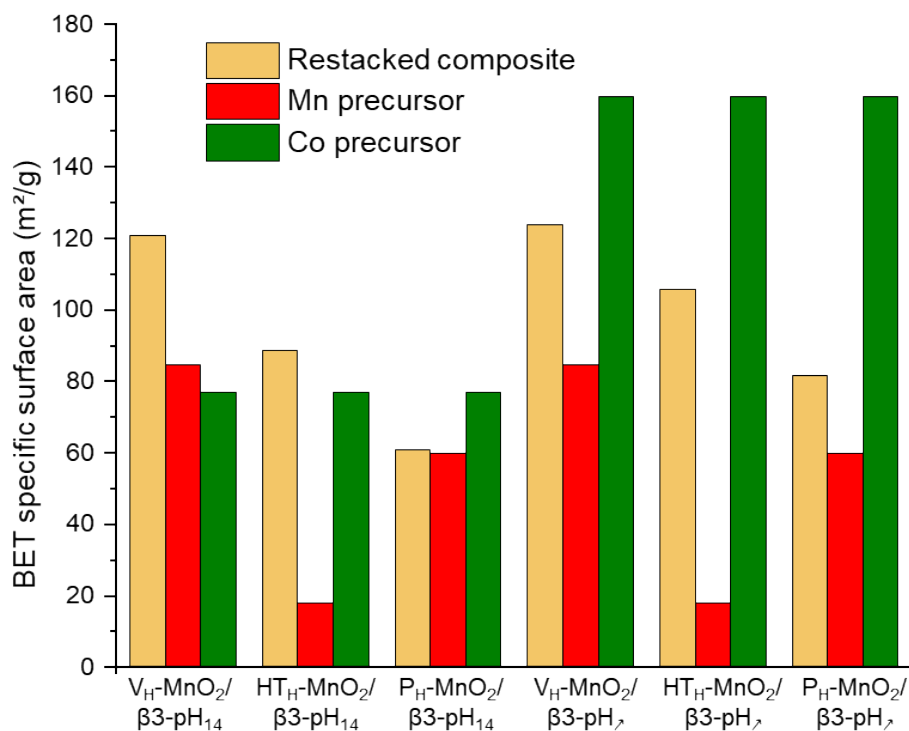


Figure 3 : A comparison of the specific surface area of the six different composites (in beige) with their Manganese and Cobalt precursors (in red and green respectively).

2) Morphology of the restacked materials compared to their precursors

In parallel to the structural investigation, a microscopic study was performed to characterize the particle shape and size of all the manganese and cobalt precursors (Figure 4) and evaluate the impact of the different exfoliation/restacking processes on the obtained composites (Figure 5).



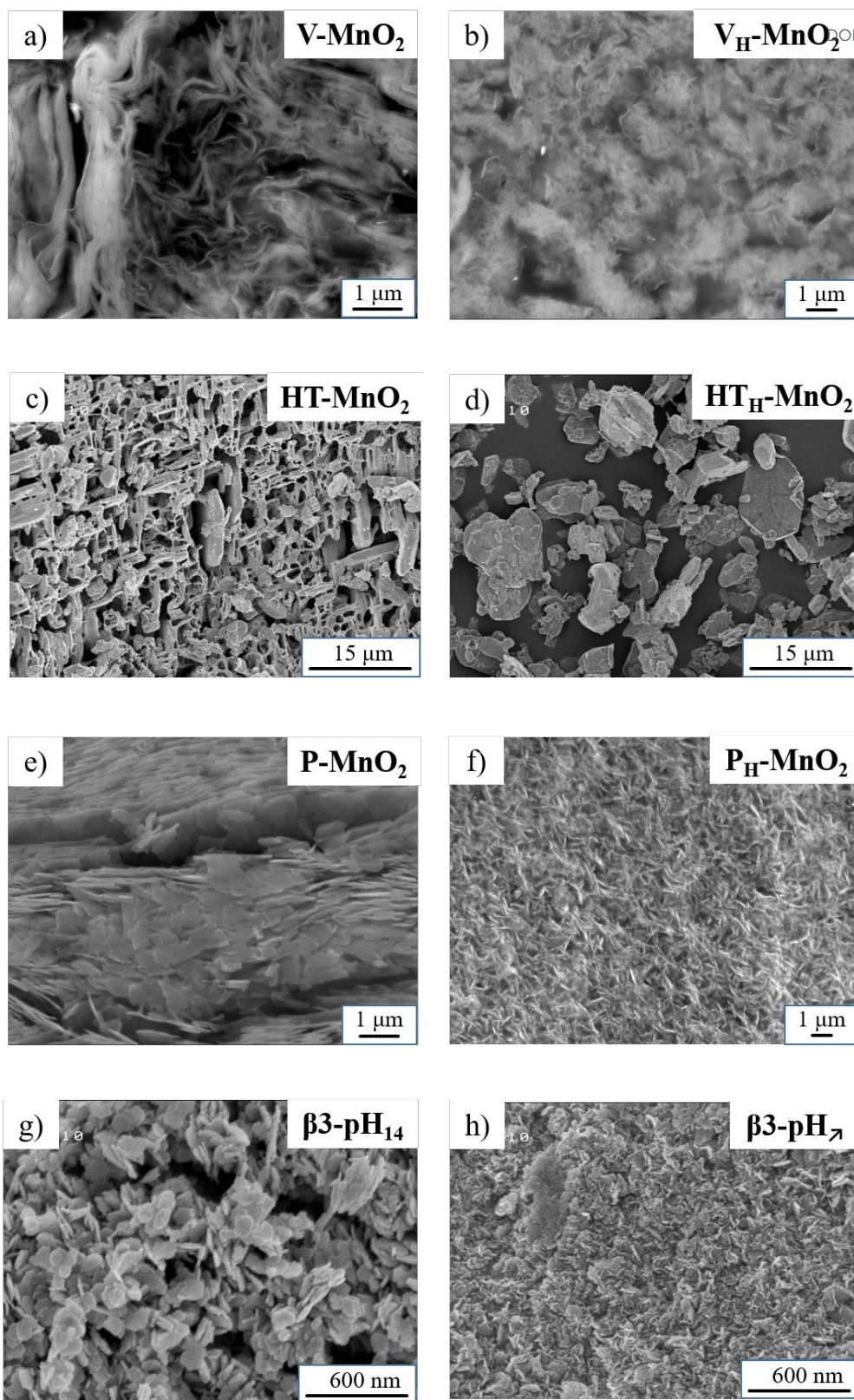


Figure 4 : SEM images of the various manganese oxides a) $V\text{-MnO}_2$, b) $V_H\text{-MnO}_2$, c) $HT\text{-MnO}_2$, d) $HT_H\text{-MnO}_2$, e) $P\text{-MnO}_2$, f) $P_H\text{-MnO}_2$ and cobalt oxyhydroxide precursors g) $\beta 3\text{-pH}_{14}$, and h) $\beta 3\text{-pH}_7$.



The SEM image of V-MnO₂ (Figure 4a) shows that the material is composed by randomly aggregated veils with a size estimated around few micrometers wide and a thickness of several ten of nanometers. After protonation, the veil morphology is preserved for V_H-MnO₂ but its size is reduced down to 1 μm (Figure 4b). The acidic treatment probably leads to break and/or disperse the veils, which consequently decrease their size.

The other two birnessites HT-MnO₂ and P-MnO₂ are constituted by platelets. HT-MnO₂ is characterized by a 3D network of interconnected platelets that are 1-2 μm thick and 10 μm wide, leading to large cavities within the material (Figure 4c). The protonation does not influence the platelet's size nor morphology. On the other hand, the 3D network disappears and the platelets are found disconnected and isolated from each other (Figure 4d). Finally, SEM image of P-MnO₂ (Figure 4e) displays a stacking of platelets that are globally smaller and thinner than for HT-MnO₂ and measuring around 1 μm wide. After the protonation step, the platelets of P_H-MnO₂ (Figure 4f) appear smaller both in wide and in thickness, which is in good agreement with the exfoliation deduced previously from the decrease of coherent domain sizes and the possible particle erosion in the acid medium.

The two cobalt oxyhydroxide precursors β3-pH₁₄ and β3-pH₇ possess both a platelet morphology but a different particle size. β3-pH₁₄ is characterized by randomly aggregated and well-defined hexagonal platelets measuring 60 -100 nm wide (Figure 4g) whereas they are less defined and around 20-30 nm for β3-pH₇. (Figure 4h).

After the exfoliation/restacking processes, transmission electron microscopy (TEM) images clearly demonstrate that all the composites are characterized by a mixture of particles presenting similar morphologies than that of their corresponding protonated precursors (Figure 5). TEM images of the three composites obtained with β3-pH₁₄ (Figure 5a, c) and e)) clearly display the hexagonal platelets of β3-pH₁₄ (surrounded in green) measuring approximately 60-90 nm. In parallel, clusters of small platelets measuring around 20-30 nm and characteristic of β3-pH₇ can also be identified (green color) for the three other composites on the figure 5b), d) and f). On Figure 5a) and 5b), veils of V_H-MnO₂ can be distinguished but the evaluation of their size is difficult especially because the veils are rolling up on themselves and are heterogeneous in size (from ten to several hundreds of nanometers wide). Nevertheless, the presence of very small and thin particles after restacking suggests that V_H-MnO₂ was exfoliated as previously mentioned.



Finally, platelet shape particles of $\text{HT}_{\text{H}}\text{-MnO}_2$ and $\text{P}_{\text{H}}\text{-MnO}_2$ precursors can be identified in $\text{HT}_{\text{H}}\text{-MnO}_2/\beta 3\text{-pH}_{14}$ // $\text{HT}_{\text{H}}\text{-MnO}_2/\beta 3\text{-pH}_7$ (Figure 5c and 5d) and $\text{P}_{\text{H}}\text{-MnO}_2/\beta 3\text{-pH}_{14}$ // $\text{P}_{\text{H}}\text{-MnO}_2/\beta 3\text{-pH}_7$ (Figure 5e and 5f) composites respectively. However, the primary particles of $\text{HT}_{\text{H}}\text{-MnO}_2$ appear thinner and smaller in the restacked composites compared to those observed for $\text{HT}_{\text{H}}\text{-MnO}_2$ before restacking (Figure 4d), supporting that an exfoliation occurred. On the other hand, the platelets of $\text{P}_{\text{H}}\text{-MnO}_2$, which measure 500-600 nm wide, maintain the same size. To summarize, the morphology of the cobalt and manganese primary particle precursors is maintain within the restacked materials and the evolution of the particle size is in good agreement with the observations made from the evolution of coherent domains and specific surface areas. $\text{HT}_{\text{H}}\text{-MnO}_2$ and $\text{V}_{\text{H}}\text{-MnO}_2$ were exfoliated during the synthesis of composites whereas the primary platelets of $\text{P}_{\text{H}}\text{-MnO}_2$, $\beta 3\text{-pH}_{14}$ and $\beta 3\text{-pH}_7$ were just dispersed.

View Article Online
DOI: 10.1039/D2NA00616B



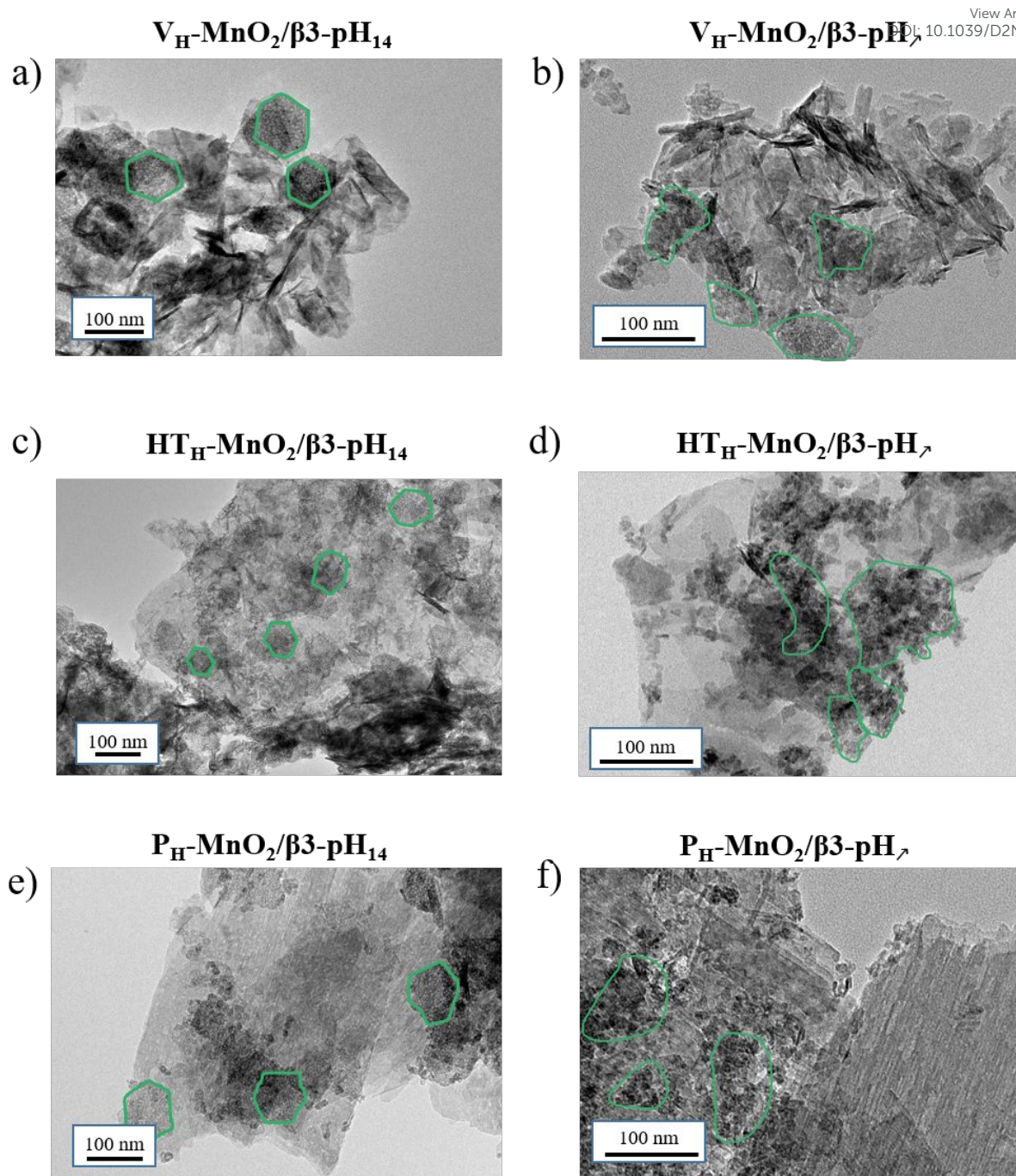


Figure 5 : TEM images of the various restacked materials a) $V_H\text{-MnO}_2/\beta 3\text{-pH}_{14}$, b) $V_H\text{-MnO}_2/\beta 3\text{-pH}_7$, c) $HT_H\text{-MnO}_2/\beta 3\text{-pH}_{14}$, d) $HT_H\text{-MnO}_2/\beta 3\text{-pH}_7$, e) $P_H\text{-MnO}_2/\beta 3\text{-pH}_{14}$, f) $P_H\text{-MnO}_2/\beta 3\text{-pH}_7$.

3) Distribution of the Mn and Co objects within the restacked composites using Auger Spectroscopy



After evaluating the size and shape of primary particles before and after restacking, nano-Auger analyses were performed to get information on the distribution scale of the Mn and Co objects within the aggregates. For that, SEM images, AES spectra and SAM images (elemental 2D distribution) were acquired on cross section of the composites as prepared by ion milling and are presented in Figure 6 and S4-S6. The nanometric probe size for AES (20 nm wide and 3 nm deep, i.e. about 30 nm spatial resolution for SAM images) gives the possibility to determine if the composites are assembled at a nanometric scale by the simultaneous presence of Mn and Co transitions in the Auger spectrum.

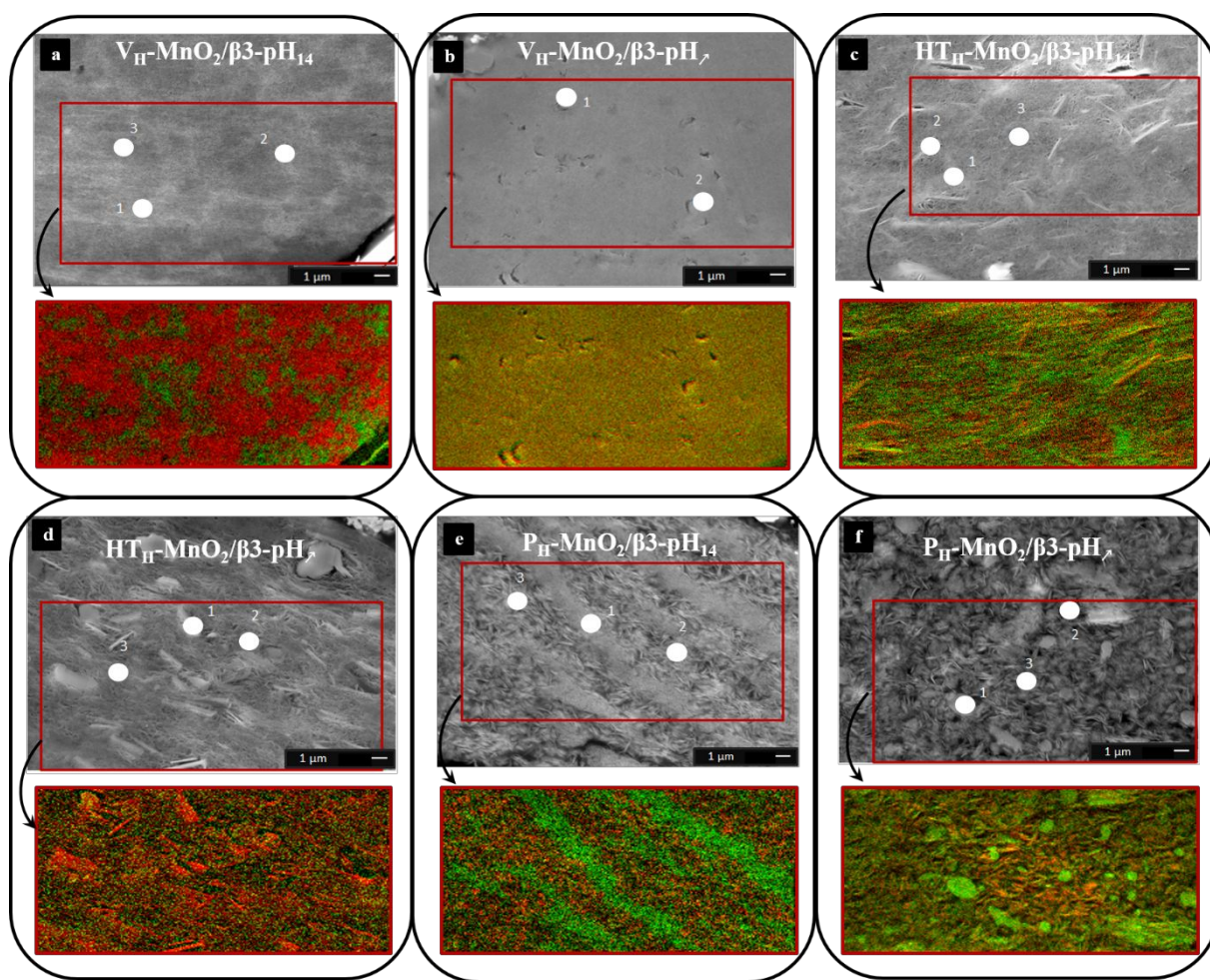


Figure 6: SEM image and SAM image (Mn in red and Co in green) of (a) $V_H\text{-MnO}_2/\beta 3\text{-pH}_{14}$ (b) $V_H\text{-MnO}_2/\beta 3\text{-pH}_7$ (c) $HT_H\text{-MnO}_2/\beta 3\text{-pH}_{14}$ (d) $HT_H\text{-MnO}_2/\beta 3\text{-pH}_7$ (e) $P_H\text{-MnO}_2/\beta 3\text{-pH}_{14}$ (f) $P_H\text{-MnO}_2/\beta 3\text{-pH}_7$.

For the two composites based on the $V_H\text{-MnO}_2$ material (Figure 6), the SEM images show a very different structure in the bulk of the aggregates. For the restacked $V_H\text{-MnO}_2/\beta 3\text{-pH}_{14}$ material (Figure 6a), two shades of grey are observed while for the $V_H\text{-MnO}_2/\beta 3\text{-pH}_7$ material



(Figure 6b) the bulk structure is more uniform. For both samples, the porosity seems low and relatively homogeneous while the manganese or cobalt particles are not visible.

For the $V_{\text{H}}\text{-MnO}_2/\beta\text{3-pH}_{14}$ (Figure 6a), the analysis points performed in the brighter areas (point 1 and 2) shows the presence of the Mn LMM and the Co LMM transitions (Figure S4). On the other hand, for the analysis point 3, there is only the Mn LMM transition. The SAM image (Figure 6a) confirm the results obtained with the Auger spectra by the presence of Mn rich domains in red and Co rich domains in green. Each domain measures few micrometers and Mn-rich areas appear larger than Co ones due to the higher amount of manganese in the composite (Molar ratio Mn:Co = 3). For $V_{\text{H}}\text{-MnO}_2/\beta\text{3-pH}_{\lambda}$, the Auger spectra show the simultaneous presence of the Mn LMM and Co LMM transitions (point 1 and 2) (Figure S4). Concerning the SAM image (Figure 6b), there is no visible domain, the totality of the image is yellow, which corresponds to the mixture of red (Mn) and green (Co) suggesting a very homogeneous distribution at nanoscale.

For the two composites obtained with $\text{HT}_{\text{H}}\text{-MnO}_2$, $\text{HT}_{\text{H}}\text{-MnO}_2/\beta\text{3-pH}_{14}$ (Figure 6c) and $\text{HT}_{\text{H}}\text{-MnO}_2/\beta\text{3-pH}_{\lambda}$ (Figure 6d), the manganese oxide platelets of several micrometers wide are clearly visible on the SEM images. Probably due to the huge difference in particle size between Co and Mn objects leading to less compact stacking, SEM images suggest a higher macroporosity within the composites than for those with $V_{\text{H}}\text{-MnO}_2$ (Figure 6a and 6b). Auger spectra performed for the $\text{HT}_{\text{H}}\text{-MnO}_2/\beta\text{3-pH}_{14}$ composite on brighter areas/platelets at point 1 and 2 show the presence of mainly Mn LMM transitions while Co LMM transitions are barely visible or even absent (Figure S5). On the other hand, the analysis at point 3, performed on a dark grey area that looks like $\beta\text{3-pH}_{14}$ material, shows the simultaneous presence of Mn LMM and Co LMM transitions. Considering the analysis depth of 3 nm, it means that manganese oxide platelets can be probed below the $\beta\text{3-pH}_{14}$. The same observations/conclusions are obtained for the $\text{HT}_{\text{H}}\text{-MnO}_2/\beta\text{3-pH}_{\lambda}$ composite from SEM image and Auger spectra (Figure S5). SAM images for both composites clearly expose $\text{HT}_{\text{H}}\text{-MnO}_2$ platelets in red or with some yellow part corresponding to the presence of both manganese and cobalt (Figure 6c and 6d). The cobalt represented by the green color is also detected rather homogeneously on the whole samples.

For the last two composites obtained with $\text{P}_{\text{H}}\text{-MnO}_2$, the bulk structure is very different. $\text{P}_{\text{H}}\text{-MnO}_2/\beta\text{3-pH}_{14}$ differs completely from the other restacked materials when focusing on the distribution of the Mn and Co objects that make the composites. SEM image (Figure 6e) shows “line shape” domains extending over several micrometers that correspond solely to $\text{P}_{\text{H}}\text{-MnO}_2$



or $\beta 3\text{-pH}_{14}$, as highlighted on the mapping with well-defined red and green areas. The Auger spectra support this heterogeneous distribution between Mn and Co objects. Only Co LMM transitions are detected at point 1 whereas the Auger spectra at points 2 and 3 highlight only the presence of Mn LMM transitions (Figure S6). SAM (Figure 6e) reveals the absence of area containing both Mn and Co objects (yellow color).

On the other hand, such consequent heterogeneities between cobalt and manganese phases are not observed for the $\text{P}_\text{H}\text{-MnO}_2/\beta 3\text{-pH}_7$ and SEM image (Figure 6f) shows only platelets arranged with random orientation. The AES spectra of point 1 and 2 show the simultaneous presence of the Mn LMM and Co LMM transitions with a higher intensity of the Co LMM transitions than for Mn LMM transitions (Figure S6). On the other hand, in the spectrum of point 3, only the Mn LMM transitions are visible. The SAM image made on this sample highlights the fact that Mn and Co are not present in the whole sample (Figure S6).

To summarize, the six composites obtained and analysed have each a different arrangement between the Co and Mn objects depending on the morphology of the precursors. $\text{P}_\text{H}\text{-MnO}_2/\beta 3\text{-pH}_{14}$ clearly shows that the manganese and cobalt objects are not well mixed. It presents the worst distribution homogeneity within the series and is considered as a simple composite. Then, $\text{V}_\text{H}\text{-MnO}_2/\beta 3\text{-pH}_{14}$, $\text{P}_\text{H}\text{-MnO}_2/\beta 3\text{-pH}_7$, $\text{HT}_\text{H}\text{-MnO}_2/\beta 3\text{-pH}_{14}$ and $\text{HT}_\text{H}\text{-MnO}_2/\beta 3\text{-pH}_7$ seem to show similar distribution between the objects at both micro and nano scales. All these composites possess areas where both cobalt and manganese were simultaneously detected and other areas where only manganese is present. These four compounds are thus defined as micro-composites. Finally, $\text{V}_\text{H}\text{-MnO}_2/\beta 3\text{-pH}_7$ definitely reveals the best distribution homogeneity between the Co and Mn objects at the nano scale and is considered as a nano-composite. Thus, combining the BET surface area results with the observations made by nano-Auger analysis, $\text{V}_\text{H}\text{-MnO}_2/\beta 3\text{-pH}_7$ stands out from the others due to its distribution of Co and Mn objects at the nanoscale, its high mesoporosity and specific surface area. It will be thus very interesting to compare its energy storage performance to the other composites of the series.



4) Electrochemical behaviour and performances

View Article Online
DOI: 10.1039/D2NA00616B

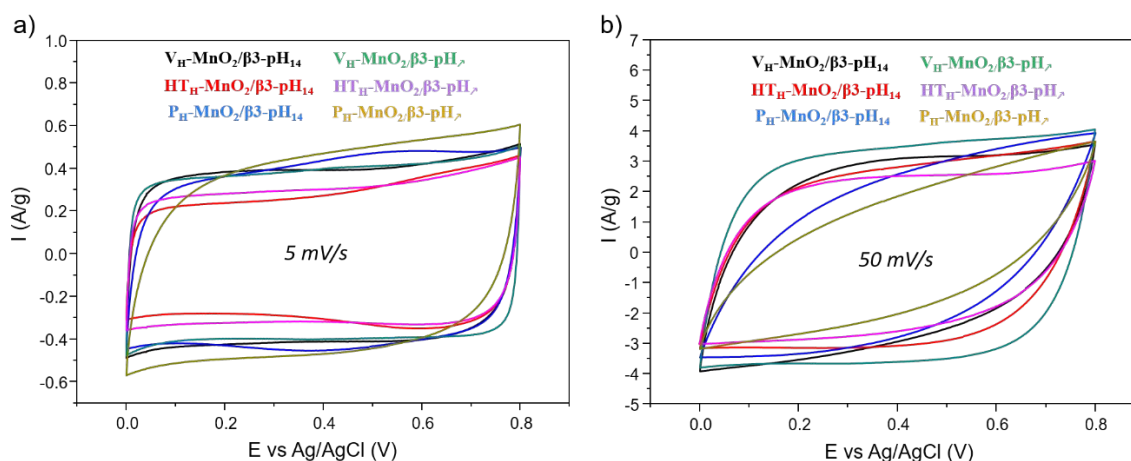


Figure 7 : Cyclic voltammetry of various restacked composites in 0.5 M K_2SO_4 at a) 5 mV/s and b) 50 mV/s : $V_H-MnO_2/\beta 3-pH_{14}$ (black), $HT_H-MnO_2/\beta 3-pH_{14}$ (red), $P_H-MnO_2/\beta 3-pH_{14}$ (blue), $V_H-MnO_2/\beta 3-pH_\gamma$ (green), $HT_H-MnO_2/\beta 3-pH_\gamma$ (purple), $P_H-MnO_2/\beta 3-pH_\gamma$ (yellow).

To investigate the impact of the precursor's morphology on the energy storage performance of restacked materials, cyclic voltammetry, galvanostatic charge/discharge and impedance spectroscopy measurements were performed on electrodes with active mass loading of ~ 10 mg/cm². The voltammograms recorded at 5 mV/s for all composites (Figure 7a) show a rectangular shape characteristic of a pseudocapacitive behavior, such as for protonated manganese oxides and contrary to the initial MnO_2 compounds that show redox peaks (Figure S7), usually attributed to the intercalation/dintercalation of alkaline ions. Those redox peaks disappear after protonation because most probably the H^+ , localized in tetragonal sites near from the manganese oxide slabs, are not exchangeable and prevent the intercalation of the alkaline ions.^{41,42}

At 50 mV/s (Figure 7b), $V_H-MnO_2/\beta 3-pH_\gamma$ stands out from the other restacked materials by keeping a very rectangular shape whereas the CV profile of the other composites become elliptic, especially for $P_H-MnO_2/\beta 3-pH_\gamma$ and $P_H-MnO_2/\beta 3-pH_{14}$. These comparisons suggest that at high sweep rate, the $V_H-MnO_2/\beta 3-pH_\gamma$ nano-composite possesses the lowest resistivity among the composite series. It can be correlated to the observations made by microscopy and especially by nano-Auger, which reveal that, contrary to the other restacked materials that are composites or micro composites, only $V_H-MnO_2/\beta 3-pH_\gamma$ is a nano composite with a homogenous distribution between Co and Mn objects at the nanoscale. The closer interaction between pseudocapacitive V_H-MnO_2 and electronic conductor $\beta 3-pH_\gamma$ in $V_H-MnO_2/\beta 3-pH_\gamma$



results in a more efficient synergy leading to a less resistive behavior at high scan rate (Figure 7b).

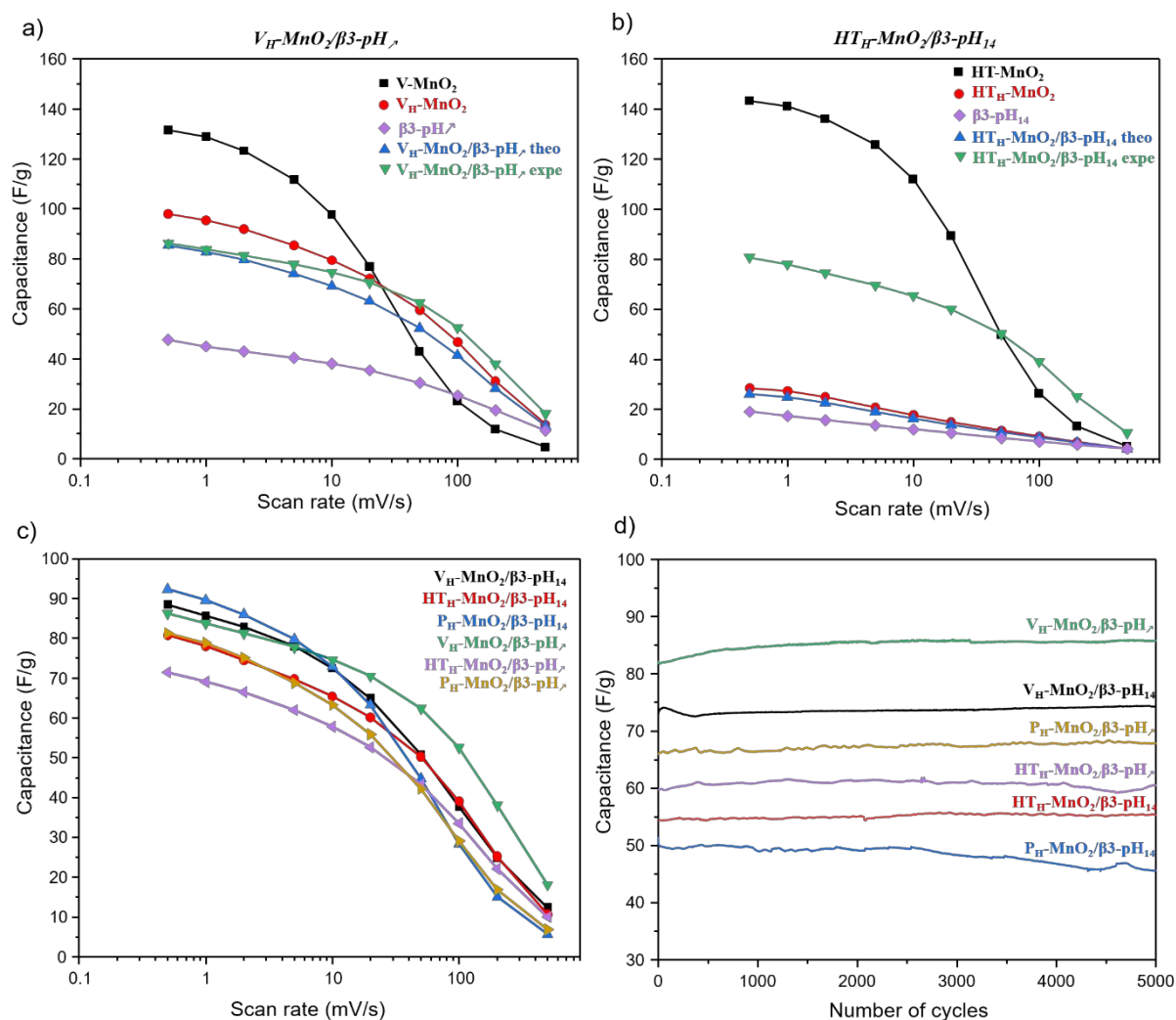


Figure 8 : a) Capacitance vs scan rate of various restacked materials. Comparison of the capacitance at different scan rates for the precursors constituting the restacked material with the theoretical and experimental capacitance of b) $V_{H^-}MnO_2/\beta 3-pH_7$ and c) $HT_{H^-}MnO_2/\beta 3-pH_{14}$ d) Cyclability of the composites in galvanostatic mode at 1 A/g on the potential window 0-0.8 V vs Ag/AgCl in 0.5 M K_2SO_4 : $V_{H^-}MnO_2/\beta 3-pH_{14}$ (black), $HT_{H^-}MnO_2/\beta 3-pH_{14}$ (red), $P_{H^-}MnO_2/\beta 3-pH_{14}$ (blue), $V_{H^-}MnO_2/\beta 3-pH_7$ (green), $HT_{H^-}MnO_2/\beta 3-pH_7$ (purple), $P_{H^-}MnO_2/\beta 3-pH_7$ (yellow).

First, in order to show the interest of making restacked composite materials, it is relevant to compare their performance to those of their precursors. We can clearly see that in K_2SO_4 electrolyte, the electrochemical activity of MnO_2 is much higher than that of H_xCoO_2 . Additionally, in all composites there are 3 times more MnO_2 than H_xCoO_2 . Thus, H_xCoO_2 is mainly likely to bring electrical conductivity while its contribution to charge storage is very limited in the composite. The whole manganese oxide precursors exhibit a similar variation of



capacity as a function of rate (Figure 8a), 8b) and Figure S7). At low scan rates, the capacities overcome 100 F/g before strongly decreasing beyond 20 mV/s. Indeed, the faradaic charge storage mechanism, predominant at low rates, is kinetically limited at higher rates, where capacitive storage is favored. Compared to these alkaline manganese oxide precursors, the composites including $V_H\text{-MnO}_2$, as well as for the $HT_H\text{-MnO}_2/\beta 3\text{-pH}_{14}$, exhibit at high rate a higher specific capacity (green curve), which justifies the interest of these composites. On the contrary, it is not the case for the composites based on a $P_H\text{-MnO}_2$ precursor with platelet morphology, nor for the $HT_H\text{-MnO}_2/\beta 3\text{-pH}_7$ material, which all three exhibit a capacity lower than that of the Mn precursors, whatever the rate. Additionally, it is important to note that, whatever the rate, all the composites present better experimental capacities than the theoretical ones, calculated considering the weighted average capacity of Co and Mn precursors (see Figure S8 for more details). These results clearly prove a real synergy effect between both phases within the composites.

The comparison of rate capability performance within the series of restacked materials (Figure 8c) shows that, at the lowest scan rate, the capacities stay in the range 72-94 F/g; the relative differences between the most performant materials, i.e. the composites based on a Mn precursor with veal morphology and $P_H\text{-MnO}_2/\beta 3\text{-pH}_{14}$, are not really significant. On the contrary, the behavior of $V_H\text{-MnO}_2/\beta 3\text{-pH}_7$ is clearly outstanding at higher sweep rate, with a capacity that is twice that observed for the other composites at 200 mV/s. In the performance order at high rate, $V_H\text{-MnO}_2/\beta 3\text{-pH}_7$ is above $V_H\text{-MnO}_2/\beta 3\text{-pH}_{14}$ and the composites containing $HT_H\text{-MnO}_2$ precursors that are all three at the same level and finally the composites based on the $P_H\text{-MnO}_2$ precursor with platelet morphology possess the worst performance. The decreasing order of the capacities seems to follow the decreasing evolution of the specific surface areas, the $P_H\text{-MnO}_2/\beta 3\text{-pH}_{14}$ and $P_H\text{-MnO}_2/\beta 3\text{-pH}_7$ composites exhibiting the lowest SSA with 61 and 82 m^2/g respectively, and exhibiting the most inhomogeneous distribution of the 2 components. Although the different composites display various rate capability, no capacity loss is observed after 5000 cycles for all of them, which reveals that the association of cobalt oxyhydroxide and manganese oxide within a composite via an exfoliation/restacking process leads to stable materials during electrochemical cycling in K_2SO_4 , thanks to a good cohesion between the objects, whose morphologies do not affect the stability (Figure 8d). It should be noted that, as shown in previous study reported by Tang et al.,²⁸ a simple mixture between the precursors did not lead to an optimal cohesion, entailing thus a capacity drop from the first 100 cycles, which is completely avoided by using composites prepared by exfoliation/restacking.



It can therefore be concluded that the very homogeneous organization of the Mn and Co objects at the nanoscale, previously evidenced by nano-Auger analysis, its mesoporosity as well as its highest specific surface area allow $V_H\text{-MnO}_2/\beta\text{3-pH}_7$ to reach the best performance among the other studied composites.

In order to confirm the influence of the morphology and of the distribution scale homogeneity of the objects contained in the restacked materials, an electrochemical impedance spectroscopy study has been carried out on $V_H\text{-MnO}_2/\beta\text{3-pH}_7$ nanocomposite, presenting the rate capability performance, in comparison with the $HT_H\text{-MnO}_2/\beta\text{3-pH}_{14}$ microcomposite, whose capacity is just lower at high rate.

The spectra and fitted data according to the equivalent circuit presented Figure S9 show similar values for all the working potentials as presented in supplementary Figure S10 and Table S3. In the manuscript, only the spectra at 0.3 V are represented in Figure 9 for clarity. The potential variation has no influence on the loop of the spectra at high frequencies (Figure S10), which allows to attribute the resistance R_2 characterized by a semi-circle to the electric percolation within the material. This weaker resistance observed for $V_H\text{-MnO}_2/\beta\text{3-pH}_7$ compared to $HT_H\text{-MnO}_2/\beta\text{3-pH}_{14}$ (3.4 Ohm against 4.2 Ohm) reveals a better percolation between the grains for the former material, as it was expected due to a better homogeneity between Co and Mn objects. Indeed, the veal morphology of the Mn objects is likely to wrap up as much as possible the Co oxyhydroxide platelets, leading therefore to an optimal interaction promoting the electronic transfers in $V_H\text{-MnO}_2/\beta\text{3-pH}_7$. Regarding the ionic diffusion, the S2 impedance is also lower for $V_H\text{-MnO}_2/\beta\text{3-pH}_7$.

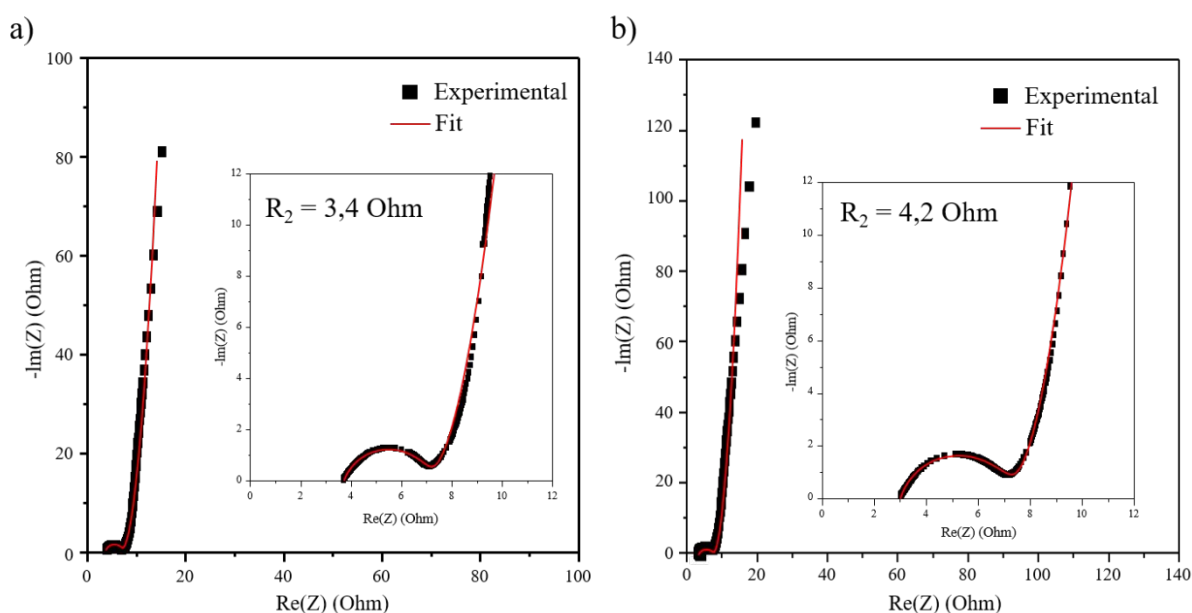


Figure 9 : Nyquist plots of the restacked materials a) $V_H\text{-MnO}_2/\beta\text{-pH}_\lambda$, b) $HT_H\text{-MnO}_2/\beta\text{-pH}_\lambda$ at 0.3 V.

View Article Online
DOI: 10.1039/D2NA00616B



Conclusion

View Article Online
DOI: 10.1039/D2NA00616B

This work was focused on the influence of the morphology of composites synthesized by exfoliation/restacking of cobalt oxyhydroxides and birnessite manganese dioxides on their electrochemical properties. Starting from birnessite phases with different morphologies (veals, nanoplatelets and microplatelets) associated with 2 cobalt oxyhydroxides (platelets with different sizes), 6 different composites are obtained, with the same Mn:Co ratio fixed to 3:1.

Nano-Auger analysis turned out to be a key tool to identify the distribution scale of the Mn and Co objects within the restacked composites, depending on the morphology of the precursors and their interaction. The materials that are based on manganese oxide with platelet morphology appear as composites at the micrometric scale, and even beyond, with significant inhomogeneities when the Mn platelets are nanometric. On the other hand, the materials containing the manganese oxide component with veal morphology exhibit a very intimate mixture between the Co and Mn-based objects. The combination of the veal Mn morphology with the smallest nanoplatelets of cobalt oxyhydroxide allows obtaining the best distribution of the objects, leading to a nanocomposite. This material has the highest specific surface among the composites (124 m²/g) and leads to the best capacitance, 84 F/g at 1 A/g after 5000 cycles for electrode with 10 mg/cm² mass loading. The EIS measurements show a lower resistance and a better inter-grain percolation for this material. The synergy between the conductive cobalt oxyhydroxide platelets and the pseudocapacitive manganese oxide veals is effective in this material.

Acknowledgment:

The authors would like to thank AID as well as Bordeaux INP for financial support (PhD funding and research fees). The authors thank also Région Nouvelle Aquitaine and the French National Research Agency (STORE-EX Labex Project ANR-10-LABX-76-01) for financial support and fruitful discussions. Many thanks to Catherine Denage, Emmanuel Petit, Eric Lebraud for their help in the characterization of the samples for ICP, MEB and XRD.



Reference:

View Article Online
DOI: 10.1039/D2NA00616B

- 1 J. Ma, Y. Li, N. S. Grundish, J. B. Goodenough, Y. Chen, L. Guo, Z. Peng, X. Qi, F. Yang, L. Qie, C.-A. Wang, B. Huang, Z. Huang, L. Chen, D. Su, G. Wang, X. Peng, Z. Chen, J. Yang, S. He, X. Zhang, H. Yu, C. Fu, M. Jiang, W. Deng, C.-F. Sun, Q. Pan, Y. Tang, X. Li, X. Ji, F. Wan, Z. Niu, F. Lian, C. Wang, G. G. Wallace, M. Fan, Q. Meng, S. Xin, Y.-G. Guo and L.-J. Wan, *J. Phys. D. Appl. Phys.*, 2021, **54**, 183001.
- 2 J. Amici, P. Asinari, E. Ayerbe, P. Barboux, P. Bayle-Guillemaud, R. J. Behm, M. Bercibar, E. Berg, A. Bhowmik, S. Bodoardo, I. E. Castelli, I. Cekic-Laskovic, R. Christensen, S. Clark, R. Diehm, R. Dominko, M. Fichtner, A. A. Franco, A. Grimaud, N. Guillet, M. Hahlin, S. Hartmann, V. Heiries, K. Hermansson, A. Heuer, S. Jana, L. Jabbour, J. Kallo, A. Latz, H. Lorrman, O. M. Løvvik, S. Lyonnard, M. Meeus, E. Paillard, S. Perraud, T. Placke, C. Punckt, O. Raccurt, J. Ruhland, E. Sheridan, H. Stein, J. Tarascon, V. Trapp, T. Vegge, M. Weil, W. Wenzel, M. Winter, A. Wolf and K. Edström, *Adv. Energy Mater.*, 2022, **2102785**, 2102785.
- 3 J. Janek and W. G. Zeier, *Nat. Energy*, 2016, **1**, 1–4.
- 4 S. Liu, L. Kang, J. Zhang, S. C. Jun and Y. Yamauchi, *ACS Energy Lett.*, 2021, **6**, 4127–4154.
- 5 M. Yassine and D. Fabris, *Energies*, 2017, **10**, 1340–1351.
- 6 Y. Jiang and J. Liu, *ENERGY Environ. Mater.*, 2019, **2**, 30–37.
- 7 Y. Gogotsi and R. M. Penner, *ACS Nano*, 2018, **12**, 2081–2083.
- 8 S. Fleischmann, J. B. Mitchell, R. Wang, C. Zhan, D. Jiang, V. Presser and V. Augustyn, *Chem. Rev.*, 2020, **120**, 6738–6782.
- 9 C. Julien and A. Mauger, *Nanomaterials*, 2017, **7**, 396.
- 10 M. Huang, F. Li, F. Dong, Y. X. Zhang and L. L. Zhang, *J. Mater. Chem. A*, 2015, **3**, 21380–21423.
- 11 T. Brousse, P.-L. Taberna, O. Crosnier, R. Dugas, P. Guillemet, Y. Scudeller, Y. Zhou, F. Favier, D. Bélanger and P. Simon, *J. Power Sources*, 2007, **173**, 633–641.
- 12 A. Boisset, L. Athouël, J. Jacquemin, P. Porion, T. Brousse and M. Anouti, *J. Phys. Chem. C*, 2013, **117**, 7408–7422.



- 13 S. Zhu, W. Huo, X. Liu and Y. Zhang, *Nanoscale Adv.*, 2020, **2**, 37–54. View Article Online
DOI: 10.1039/D2NA00616B
- 14 S. Liu, L. Kang and S. C. Jun, *Adv. Mater.*, 2021, **33**, 1–40.
- 15 E. Pomerantseva, F. Bonaccorso, X. Feng, Y. Cui and Y. Gogotsi, *Science (80-.)*, 2019, **366**, eaan8285.
- 16 Y. Fu, X. Gao, D. Zha, J. Zhu, X. Ouyang and X. Wang, *J. Mater. Chem. A*, 2018, **6**, 1601–1611.
- 17 E. Eustache, C. Douard, R. Retoux, C. Lethien and T. Brousse, *Adv. Energy Mater.*, 2015, **5**, 3–7.
- 18 H. Liu, W. Gu, B. Luo, P. Fan, L. Liao, E. Tian, Y. Niu, J. Fu, Z. Wang, Y. Wu, G. Lv and L. Mei, *Electrochim. Acta*, 2018, **291**, 31–40.
- 19 C. C. H. Tran, J. Santos-Peña and C. Damas, *J. Phys. Chem. C*, 2018, **122**, 16–29.
- 20 H. Xia, X. Zhu, J. Liu, Q. Liu, S. Lan, Q. Zhang, X. Liu, J. K. Seo, T. Chen, L. Gu and Y. S. Meng, *Nat. Commun.*, 2018, **9**, 5100.
- 21 Z.-H. Huang, Y. Song, D.-Y. Feng, Z. Sun, X. Sun and X.-X. Liu, *ACS Nano*, 2018, **12**, 3557–3567.
- 22 D. Wu, X. Xie, Y. Zhang, D. Zhang, W. Du, X. Zhang and B. Wang, *Front. Mater.*, 2020, **7**, 1–16.
- 23 Q.-Z. Zhang, D. Zhang, Z.-C. Miao, X.-L. Zhang and S.-L. Chou, *Small*, 2018, **14**, 1702883.
- 24 Z. Su, C. Yang, C. Xu, H. Wu, Z. Zhang, T. Liu, C. Zhang, Q. Yang, B. Li and F. Kang, *J. Mater. Chem. A*, 2013, **1**, 12432.
- 25 J. Kang, A. Hirata, L. Kang, X. Zhang, Y. Hou, L. Chen, C. Li, T. Fujita, K. Akagi and M. Chen, *Angew. Chemie Int. Ed.*, 2013, **52**, 1664–1667.
- 26 R. B. Rakhi, B. Ahmed, D. Anjum and H. N. Alshareef, *ACS Appl. Mater. Interfaces*, 2016, **8**, 18806–18814.
- 27 S. Zhu, Q. Shan, F. Dong, Y. Zhang and L. Zhang, *Gold Bull.*, 2017, **50**, 61–68.
- 28 C. Tang, D. Giaume, F. Weill, N. Penin, M.-A. Dourges, H. Saadaoui and L. Guerlou-Demourgues, *ACS Appl. Energy Mater.*, 2019, **2**, 7832–7842.



- 29 R. Invernizzi, L. Guerlou-Demourgues, F. Weill, A. Lemoine, M.-A. Dourges, I. Baraille, D. Flahaut and J. Olchowka, *Materials (Basel)*, 2021, **14**, 2325. View Article Online
DOI: 10.1039/D2NA00616B
- 30 A. Lemoine, R. Invernizzi, G. Salvato Vallverdu, L. Madec, J. Olchowka, L. Guerlou-Demourgues, I. Baraille and D. Flahaut, *J. Phys. Chem. C*, 2021, **125**, 8570–8581.
- 31 C. Tang, PhD thesis, Université de Bordeaux, 2017.
- 32 S. H. Kim, S. J. Kim and S. M. Oh, *Chem. Mater.*, 1999, **11**, 557–563.
- 33 Y. Omomo, T. Sasaki, Wang and M. Watanabe, *J. Am. Chem. Soc.*, 2003, **125**, 3568–3575.
- 34 S. Brunauer, P. H. Emmett and E. Teller, *J. Am. Chem. Soc.*, 1938, **60**, 309–319.
- 35 J. Olchowka, T. Tailliez, L. Bourgeois, M. A. Dourges and L. Guerlou-Demourgues, *Nanoscale Adv.*, 2019, **1**, 2240–2249.
- 36 E. Silvester, A. Manceau and V. A. Drits, *Am. Mineral.*, 1997, **82**, 962–978.
- 37 A.-C. Gaillot, D. Flot, V. A. Drits, A. Manceau, M. Burghammer and B. Lanson, *Chem. Mater.*, 2003, **15**, 4666–4678.
- 38 R. D. Shannon, *Acta Crystallogr. Sect. A*, 1976, **32**, 751–767.
- 39 A. G. Volkov, S. Paula and D. W. Deamer, *Bioelectrochemistry Bioenerg.*, 1997, **42**, 153–160.
- 40 S. Boyd, K. Ganeshan, W.-Y. Tsai, T. Wu, S. Saeed, D. Jiang, N. Balke, A. C. T. van Duin and V. Augustyn, *Nat. Mater.*, 2021, **20**, 1689–1694.
- 41 A. Manceau, B. Lanson and V. A. Drits, *Geochim. Cosmochim. Acta*, 2002, **66**, 2639–2663.
- 42 A.-C. Gaillot, PhD thesis, Université Joseph Fourier – Grenoble I, 2002.



Open Access Article. Published on 07 October 2022. Downloaded on 10/21/2022 3:17:43 PM.
This article is licensed under a Creative Commons Attribution-NonCommercial 3.0 Unported Licence.

